Author/s:
Kuriakose, S;Jain, SK;Tawfik, SA;Spencer, MJS;Murdoch, BJ;Singh, M;Rahman, F;Mayes, ELH;Taha, MY;Ako, RT;Bansal, V;Ahmed, T;Sriram, S;Bhaskaran, M;Balendhran, S;Walia, S

Title:
Monocrystalline Antimonene Nanosheets via Physical Vapor Deposition

Date:
2020-12-17

Citation:
Kuriakose, S., Jain, S. K., Tawfik, S. A., Spencer, M. J. S., Murdoch, B. J., Singh, M., Rahman, F., Mayes, E. L. H., Taha, M. Y., Ako, R. T., Bansal, V., Ahmed, T., Sriram, S., Bhaskaran, M., Balendhran, S. & Walia, S. (2020). Monocrystalline Antimonene Nanosheets via Physical Vapor Deposition. ADVANCED MATERIALS INTERFACES, 7 (24), https://doi.org/10.1002/admi.202001678.

Mono-crystalline antimonene nanosheets via physical vapour deposition

Sruthi Kuriakose, Shubhendra Kumar Jain, Sherif A. Tawfik, Michelle J.S Spencer, Billy J. Murdoch, Mandeep Singh, Fahmida Rahman, Edwin LH Mayes, Mohammad Yousef Taha,[†] Rajour Tanyi Ako, Vipul Bansal, Taimur Ahmed, Sharath Sriram, Madhu Bhaskaran, Sivacarendran Balendhran[††] and Sumeet Walia[†††]**

Ms Sruthi Kuriakose, Mr Shubhendra Kumar Jain, Dr Fahmida Rahman, Dr Mohammad Yousef Taha[†], Mr Rajour Tanyi Ako, Dr Taimur Ahmed, Prof Sharath Sriram, Prof Madhu Bhaskaran, Dr Sivacarendran Balendhran[††] and Assoc Prof Sumeet Walia[†††]

Functional Materials and Microsystems Research Group and the Micro Nano Research facility, RMIT University, Melbourne, VIC 3001 Australia

Dr Mohammad Yousef Taha[†] (present address)

Department of Electrical and Electronic engineering, The University of Melbourne, Parkville, VIC 3010, Australia

Dr Sivacarendran Balendhran[††] (present address)

School of Physics, The University of Melbourne, Parkville, VIC 3010, Australia

E-mail: sbalendhran@unimelb.edu.au

Assoc Prof Sumeet Walia[†††]

School of Engineering, RMIT University, Melbourne, VIC 3001 Australia

E-mail: sumeet.walia@rmit.edu.au

Dr Sherif A. Tawfik, Prof Michelle J.S Spencer

School of Science, RMIT University, Melbourne, 3001 Victoria, Australia

Dr Billy J. Murdoch, Dr Edwin LH Mayes

RMIT Microscopy and Microanalysis Facility, RMIT University, Melbourne, 3001 Australia

Dr Mandeep Singh, Prof Vipul Bansal

Ian Potter Nano Bio Sensing Facility and NanoBiotechnology Research Laboratory, School of Science, RMIT University, Melbourne VIC 3001, Australia

Keywords: antimonene, 2D materials, nanosheets, physical vapour deposition, monocrystalline

Amongst the family of elemental two-dimensional (2D) materials, antimonene is predicted to have a desirable combination of band gap tunability and exceptional physical properties. However, there is a lack of a facile synthesis technique to prepare high-quality antimonene with large aspect ratios on standard SiO_2 substrates, hindering wide scale exploration of this material. Here, we report, a physical vapour deposition process to controllably achieve millimeter- scale, β-phase, mono-crystalline antimonene nanosheets on a SiO_2 dielectric substrate. The temperature gradient across the deposition tube is exploited to realize either large-area nanosheets or single antimonene crystals on-demand. The composition and quality of the nanosheets and crystals is assessed using spectroscopy, diffraction, and microscopy techniques which suggest the formation of the β-phase allotrope. We experimentally extract the band structure of as-synthesized nanosheets which matches our theoretically calculated values. Finally, contrary to earlier reports, we reveal the oxidation of antimonene under ambient conditions over a period of time indicating the need for further experimental studies of the material's stability. The reported controllable growth of antimonene nanosheets and single crystals on conventional dielectric substrates opens a spectrum of possible applications of this material in electronics and optoelectronics devices.

1. Introduction

Many two-dimensional (2D) materials have been identified and synthesized post-graphene revolution. Synthesis of large aspect ratio 2D materials is one of the major bottlenecks towards practical deployment. The members of the 2D layered materials can be generally classified into the 2D chalcogenides, 2D oxides, and the elemental family.[1-3] The elemental family of materials has

emerged with rapidly growing interests owing to their highly tunable band gaps that span across a wide portion of the electromagnetic spectrum.[4] Layered Antimony/ene (Sb) is similar to Black phosphorus (BP) in its structure, but is projected to be stable in ambient besides being more amenable to large-scale synthesis using conventional fabrication techniques.[5-7] The partial presence of oxygen on its surface is also predicted to be a pathway for bandgap tunability.[8, 9] The band gap of monolayer antimony is estimated to be 2.28 eV,[5] filling the gap between MoS_2 (less than 2 eV) and hBN (above 5 eV).[10] Antimonene can potentially exist as a stable atomically thin two-dimensional layer, as has been confirmed by recent experimental observations [2, 11] and density functional theory (DFT) calculations.[9, 10, 12] It can possess a number of atomic structures, such as the phosphorene-like α-Sb[9-12] or silicene-like β-Sb[2, 9, 10, 12]. Their other allotropes, as discussed by Wang et al[9] are dynamically unstable.[13] Experimental investigations into the material are fairly recent and synthesis has involved epitaxial growth,[14-18] liquid-phase fabrication[19, 20] and the traditional mechanical exfoliation approaches.[2, 5] It has been found that antimony is relatively less amenable to mechanical exfoliation compared to BP, graphite or MoS_2.[21, 22] This is due to shorter out-of-plane interatomic distance in Sb making the interlayer forces stronger and therefore hindering the conventional cleavage process.[2, 5], [13] This calls for exploring the alternatives of synthesis process of the material using some of the bottom up approaches like the physical vapour deposition.

The reported synthesis using the bottom up approach of few-layer antimonene (henceforth referred as FL-Sb) crystals by far have relied on crystalline substrates such as sapphire, mica, or substrates coated with materials like Ag, $PdTe_2$, $SbTe_3$, Bi_2Te_3.[15, 17, 18, 23, 24] However, such techniques require an additional transfer processes transfer processes as demonstrated by Ji et al[18] and present scalability challenges. As a result, despite theoretical calculations that predict high carrier mobility, thermal conductivity, strain tunable electronic band structure and promising spintronic properties, reports of experimental studies on antimonene remain extremely limited, thus creating a significant knowledge gap. Hence, the next

important step is to design a scalable process to obtain either single crystals or large aspect ratio 2D antimonene on-demand.

Here, we report for the first time, to the best of our knowledge, the growth of large aspect ratio of β-phase, FL-Sb nanosheets using a physical vapour deposition technique on a SiO_2/Si substrate, a widely used CMOS-compatible substrate. This process will facilitate research into semiconductor devices based on this material. The FL-Sb nanosheets are up to 1.0 mm in lateral dimension with sub-10 nm thickness range. We further designed a temperature-gradient based control to achieve large aspect ratio growth nanosheets and single-crystals of FL-Sb in the same process. We deployed a suite of techniques to thoroughly characterize the composition, phase, crystallinity and band structure of the FL-Sb nanosheets.

2. Results and discussion

A two-zone furnace with individual temperature controls was used for the material synthesis process (schematic shown in **Figure 1a**). 0.5 mg of commercially available antimony (Sb) powder from Sigma Aldrich (99.5 % purity, 100 mesh) was used as the source material in Zone 1. The source material was vaporized at 660 ˚C. Pre cleaned SiO_2/Si (300 nm SiO_2) substrates were placed in Zone 2 at 200 ˚C for the deposition of the material. A forming gas mixture of 3% H_2/N_2 was used at a flow rate of 100 sccm as the carrier gas to carry the vapors from Zone 1 to the substrates in Zone 2. An inert mixture of gas was chosen to avoid other chemical interactions during the process. The deposition in Zone 2 took place while keeping the temperature at the center of the zone at 200 ˚C (as indicated in the schematic Figure 1a) while the pressure is maintained at 3 Torr to obtain crystals (Position 1, P1, in Figure 1a) and nanosheets (Position 2, P2 in Figure 1a) of FL-Sb. The position of the sample in Zone 2 governs the growth type/morphology (either single crystal or larger nanosheets) of the material on the substrate. This is attributed to the temperature gradient across Zone 2, where the samples are positioned. The temperature gradient of each zone in the furnace is radial from the

center to the edge. The substrate temperature primarily determines the evolution of the morphology and growth characteristics of the material on the given substrate.[25] In our case, substrates placed at two different positions (here, a temperature gradient of ±50 ˚C across the sample holder is measured with a thermocouple from the center of the Zone 2 set at 200 ˚C, indicated in Figure 1a) in Zone 2 of the furnace, provides the difference in the growth morphology. On the basis of the principle of chemical vapor deposition[25, 26], a positive temperature gradient promotes the mass transfer process of Sb vapour, forming a large amount of gaseous Sb in a short time, and thus leading to the acceleration of Sb volatilization as well as the enhancement in the growth of the crystal.[27] In our case, a relatively higher substrate temperature at P1 (250 °C), leads to high-density small nuclei[28] formation which overlaps the Sb flakes resulting in few-layer Sb crystals. In the case of Sb nanosheets at P2 (150 °C), by the oriented aggregation process[29], the Sb crystals spontaneously aggregate into large-scale few layer nanosheets of Sb. Here, the decrease in the substrate temperature leads to the formation of low-density nuclei resulting in uniform and continuous FL-Sb nanosheet.[26] Thus, the difference in the temperature gradient results in the growth of crystals and nanosheets in the same run but at two different positions (as indicated in the Figure 1a) along the furnace. The growth of the material is sensitive to the substrate temperature and the carrier gas flow rate, which is observed in this case similar to that of the growth reported for other materials such as MoS_2.[28, 30] The gas flow is kept constant maintaining the flow dynamics (gas velocity with a non-turbulent gas flow) in the furnace using mass flow controllers throughout the synthesis process. The entire synthesis process was timed for 48 min in the furnace and was then cooled down to room temperature. At the start of deposition, the epilayer atoms interact covalently with the dangling bonds of the substrate and take the lattice constant of the substrate initially, resulting in a strained epilayer.[31] However, the epilayer relaxes as the consecutive layers grow, by forming dislocations at the interface, allowing the rest of the film to grow unstrained with its natural lattice constant. In this case, the evaporated material transfers and eventually diffuses their kinetic energy on to the lattice of the substrate and readjust

themselves within the lattice during the course of the deposition process.[32] It is well known that the substrate plays one of the key roles, as it controls the adherence, nucleation and lateral growth of the material.[31] Here, SiO_2/Si substrate, a CMOS-compatible dielectric substrate is chosen for its suitability with Si-based nano-device fabrication and scalability.

The process pressure also plays a vital role as it affects the transport of the material on to the growing substrate[33] which is observed in growth of FL-Sb nanosheets and crystals. At lower pressures (<1 Torr) an overall grainy growth was observed. Usually at lower pressures the lateral growth of the nucleation sites are seemingly self-limited which is broken when pressure is increased.[34] As the pressure is increased, surface roughness of the nanosheets was observed to sequentially decrease as shown in **Figure S1**. It is known that deposition pressure is one of the factors governing the surface roughness of the grown material.[35] It is observed with previously reported synthesis of layered materials, that growth pressures >1 Torr facilitate a homogenous coverage of the material on the substrate.[31, 34] The growth of the material is typically promoted by keeping the nucleation sites density low to enable attaching to the existing nucleation sites preventing formation of another site.[31] This makes the chances of formation of new nuclei decrease further and the existing nucleation sites to grow laterally in size promoting large aspect ratio growth.[31] At an optimum pressure of 3 Torr, a homogenous growth (with an average surface roughness ~3.7 nm) at a millimetre scale lateral dimension was obtained. An optical image comparison with the bare substrate is also shown in the inset of Figure 1a, to support the same.

Atomic force microscopy (AFM) was carried out to assess the thickness and surface morphology of both the single-crystal and nanosheets of FL-Sb. **Figure 1b** and **1c** reveal a uniform surface morphology across the substrate. The thickness of the FL nanosheets are measured to be consistently sub-10 nm.

Before carrying out thorough characterizations of the as-grown nanosheets and single crystals, we theoretically assessed the atomic structural configuration of two allotropes of antimonene, as shown

in **Figure 2a, b**. We performed density functional theory (DFT) calculations to obtain the atomic and electronic structure of α-Sb and β-Sb and the lattice parameters calculated for α-Sb are *a* = 4.414 Å, *b* = 4.819 Å, α = β = γ = 90, while those of β-Sb are *a* = 4.119 Å, α=β=90, γ=120, respectively. The α-Sb has an orthorhombic structure with a direct bandgap (phosphorene-like structure) and β-Sb (silicene-like structure) has an indirect band gap (shown in **Figure 2c, d**).[9, 11, 13] The β-phase FL-Sb exhibits an ABC stacking as shown in Figure 2b (as with bulk antimony).[9] Our theoretical calculations predict an indirect bandgap of 1.25 eV for β-phase FL-Sb (Figure 2d).

Micro-Raman spectroscopy is performed on the samples to assess the quality of the synthesized material (refer to Supporting information for experimental procedure). **Figure 3a** shows the typical Raman peaks of Sb at 117 cm^{-1} and 150 cm^{-1} indicative of the E_g (in-plane) and A_{1g} (out-of-plane) phonon vibrational modes, respectively. These peaks are indicative of a β-phase growth for both FL-Sb nanosheets and single crystals.[36] There is a shift in the peaks on comparing the nanosheets and single crystals, which reflects their thickness difference. The Raman signatures of antimonene are starkly different from antimonene oxides, which indicates that the as-synthesized material is antimonene.[18, 37] Minor peaks at 190 and 255 cm^{-1} are known to appear on thin layers, due to low-level surface oxidation forming a native oxide.[18]

To assess the crystallinity of the material, we performed X-ray diffraction (XRD) analysis (**Figure 3b**) on the as-grown samples. The diffraction peaks show the presence of the characteristic (012) plane of mono-crystalline Sb (JCPDS Card No. 35-0732) suggesting a trigonal/rhombohedral structure.[38-41] The FL-Sb peaks shift from the bulk antimony is due to the increase in the interplanar spacing.[39] This also reinforces that any minuscule oxygen (which appears in the Raman spectroscopy Figure 3a) present on the surface has not altered the crystallinity of the material.

X-ray photoelectron spectroscopy (XPS) measurements confirm the presence of Sb as shown in **Figure 3c**. Sb 3*d* core-level (CL) exhibits a spin orbit splitting of ~9.4 eV for Sb $3d_{3/2}$ and Sb $3d_{5/2}$ spin states. Sb 3*d* CL is de-convoluted into Sb^0 and Sb^{3+} oxidation states which represent the antimonene

(Sb—Sb) and Sb_2O_3 chemical species, respectively. The peak positioned at 528.2±0.1 eV and 537.6±0.1 eV (associated with Sb^0) and 530.5±0.1 eV and 539.9±0.1 eV (associated with Sb^{3+}) corresponds to $3d_{5/2}$ and $3d_{3/2}$ spin states, respectively. The de-convoluted data verifies the peak values obtained for FL-Sb and it also matches the previous reports.[18, 42, 43] The peak positions of antimonene are distinct from that of the oxide (as seen clearly in Figure 3c) and hence aligns with our observations of growth of β-phase FL-Sb. The presence of Sb^{3+} state could be ascribed to the surface oxidation in the ambient conditions as native oxide which is more pronounced as the XPS is a surface sensitive tool. The additional peaks are recorded because of the overlapping of the O 1*s* CL spectra. The peaks positioned at 531.1±0.1 eV correspond to O 1*s* spectra for Sb_2O_3 which is distinct from the antimonene peaks. The 532.5±0.1 eV can be attributed to the carbon contaminants (C=O).

In the case of single crystal growth (P1 in Figure 1c), typical triangular FL-Sb crystals were observed on the SiO_2 substrate is shown in **Figure 4a**. Well-defined shape of the crystals is obtained on the SiO_2 substrate which is an indication of their crystallinity. The crystals have a lateral dimension of 100 nm to 800 nm and exhibit thicknesses that predominantly range between 10-90 nm as shown in Figure 4a and **Figure S2**. An estimate of approximately 200 single crystals in an area of 27.6 μm × 20 μm is found from the Scanning Electron Microscopy (SEM) imaging (shown in **Figure S3**), giving a choice of a range of thicknesses for further application oriented studies. An increase in the carrier gas flow rate or the amount of source material increases the thickness of the material on the substrate, as carrier gas is bound to carry more vapour to the deposition zone at a constant pressure.[44]

We investigated the structure of a single crystal using high resolution transmission electron microscopy (HRTEM). **Figure 4b** shows the HRTEM image of the crystal on the SiN grid (refer experimental section in the supporting information for more details), indicating a uniformly oriented

growth. The insets show a lattice spacing of 0.31 nm corresponding to the (012) plane of the crystal, which matches the XRD peaks obtained in this study and is in line with literature, indicative of the β-phase.[40, 45] The theoretical calculation of the lattice spacing for the (012) plane for the trigonal rhombohedral structure[46] obtained is 0.33 nm, and is in agreement with the experimentally obtained value. Fast fourier transform (FFT) is obtained from the HRTEM images shown in the Supporting information **Figure S4**, which is in line with the selected area electron diffraction (SAED) pattern obtained (shown in the inset of Figure 4b) and with previously reported literature.[40] The β-phase diffraction patterns along the (012) indicate the grown material exhibits a trigonal/rhombohedral structure that can be clearly distinguished from orthorhombic α-phase, by comparing SAED patterns in literature.[18] Electron dispersive spectroscopy (EDS) was carried out to ensure the composition of the grown material. EDS maps shown in the **Figure 4c,d** indicate concentrated presence of Sb on the crystal and oxygen content is spread across with a slight concentration on the flake region could indicate the surface oxidation correlating to the obtained Raman and XPS spectrum in Figure 3a.

Furthermore, we observed that the synthesized FL-Sb with nanometer thickness show broadband transmittance in the visible to IR range, while the optical absorbance peak occurring in the UV range (**Figure 5a**). This also suggests that the material could be used as a band reject UV filter allowing visible wavelengths to pass through. We use a combination of UV-Vis and Ultraviolet photoelectron spectroscopy (UPS) measurements to extract the band structure of the FL-Sb nanosheets. The band gap was estimated using the tauc plot (as presented in the Supporting information in the experimental section) which yields an optical band gap of 2.53 eV (shown in Figure 5a).[47] The obtained band gap values are also in the range of values obtained with our partial density of states (PDOS) and calculated band structure for the β-phase antimonene (shown in Figure 2 and Supporting information **Figure S5**) with predominant 5*p* states in valence band region. PDOS further confirms the β-phase antimonene obtained in Figure S5 which is starkly distinct from the α-phase antimonene

which has a characteristic high energy band in its conduction band that is dominated by the 4*d* orbitals.[10] Ultraviolet photoelectron spectroscopy (UPS) was performed on the grown FL-Sb and their valence band maximum values were obtained. A schematic illustrating the energy band diagram of the FL- antimonene, based on experimentally obtained values, is shown in **Figure 5b**. Previous reports have indicated that antimonene is stable under ambient conditions unlike its other elemental counterpart black phosphorus (BP). As such, we evaluate the ageing of the as-grown material by characterizing the material after 9 months using Raman spectroscopy and XPS (shown in **Figure 5c and 5d**). It is observed that with time, a significant oxide peak appears. This long-term assessment of stability has not been evaluated before.[18] The level of oxidation appears to be weaker and slower than what has been observed in black phosphorus. The developed oxide layer over the time is stable and does not degrade the material as seen in BP. From, the Raman spectra, there is a significant oxide peak at 190 and 255 cm^{-1} which persists after 9 months pointing to the oxidation of antimonene and its inability to further react with oxygen, light or humidity to structurally degrade like BP. We further observed a red-shift in the Raman peaks that are usually attributed to the shrinking of the lattice constants as the number of layers [18, 48, 49] and clearly indicate the emergence of an oxide. Similar behavioral trend is observed on the XPS of the aged sample with prominent oxide peaks at 530.5±0.1 eV and 539.9 eV±0.1 eV (associated with Sb^{3+}) corresponding to $3d_{5/2}$ and $3d_{3/2}$ spin states. The peaks are corresponding to O 1*s* spectra of Sb oxide in comparison to the freshly grown sample (Figure 5d). The UPS spectrum shown in Figure 5e,f show the predominance of the 5*p* orbital states as well denoting the growth phase of FL-Sb is not altered with the growth of oxide with time which correlates to the PDOS results. However, a surface passivation strategy may also be necessary for its deployment in practical applications. This indicates the need for further experimental investigations on intrinsic properties of FL-Sb and its interaction with the ambient.

3. Conclusion

In conclusion, we have successfully synthesized nanosheets and single crystals of antimonene on SiO_2/Si substrate, via physical vapour deposition. The material characterizations using HRTEM, optical images, Raman spectroscopy and XRD revealed that the synthesized material is β-phase, which is consistent with the atomic structure of the stable allotrope of antimonene reported in previous studies. The XPS, SEM, AFM and Raman analyses also prove that the synthesized material is homogenous on the SiO_2/Si substrate, a CMOS-compatible dielectric substrate. The experimental results agree with our theoretical calculations performed. A band structure of FL-Sb has been put forth based on experimental analysis of the band energy. Contrary to previous reports, this study also shows that FL-Sb is not stable in ambient conditions, which indicates the need for further experimental studies of the material's stability. A repeatable synthesis of sub-100 nm crystals and continuous millimeter-scale of nanosheets of FL-Sb are established on CMOS-compatible dielectric substrates. This reduces fabrication complexity by enabling direct device fabrication, which broadens the applicability of FL-Sb.

4. Experimental Section/Methods

Characterisation of antimonene

Atomic force microscopy were performed on a Veeco Dimension Icon in ScanAsyst mode. Raman spectroscopy characterizations were performed using a Horiba LabRAM HR Evolution Micro-Raman system equipped with a 532 nm laser source (50× objective). X-ray diffractograms (XRD) were collected using a Bruker D4 Endeavor XRD instrument with monochromatic Cu Kα as the radiation source, within an angular range of 2ϑ from 20° to 60°. X-ray photoelectron (XPS) measurements

were carried out using a Thermo K-Alpha XPS instrument using an Al *Kα* x-ray source (photon energy of 1486.7 eV) at a pressure of 1×10^{-9} Torr (1 Torr = 1.333×10^{2} Pa). The XPS spectra were background corrected using Shirley algorithm and the chemically distinct species were resolved using standard Gaussian-Lorentzian function. The spectra were aligned using the adventitious carbon binding energy of 284.8 eV. For XPS measurements antimonene was grown on gold-coated SiO_2/Si substrate to eliminate any interference from the substrate oxide peaks. Ultraviolet Photoelectron spectroscopy measurements were performed using a Kratos Axis Supra system equipped with He-1 (21.2 eV) and He-2 (40.8 eV) excitation energy sources. Transmission electron microscopy (TEM) was performed using a JEOL 2100F operating at 200 kV equipped with a Gatan One View camera. The grids used were with SiN membrane of 20 nm thickness and window opening of 0.5 mm. Silicon nitride (SiN) membrane grids was used as the substrate to grow the material directly on the grid to ensure non-destructive imaging. Scanning Electron Microscopy (SEM) imaging was performed using an FEI Verios 460L FESEM operating at 3 kV. The samples were prepared using standard mounting methods with carbon tape grounding strap connecting the top face the stub. A 3 nm Iridium (Ir) coating was applied to mitigate sample charging.

Density Function Theory (DFT)

Calculations were performed using density functional theory (DFT) as implemented in the Vienna *Ab initio* Simulation Package (VASP).[50] A plane-wave pseudopotential approach was used with the energy cut-off set to 500 eV. A generalised gradient approximation (GGA) in the Perdew-Burke-Ernzerhof (PBE) form was used,[51] with the ion-electron interaction defined using the projector augmented wave (PAW) method.[52] A **k**-point mesh of $1 \times 1 \times 1$ was used for geometry optimisations. The electronic self-consistent calculation is performed with an energy tolerance of 10^{-6} eV. We fully relaxed the atomic structure and the lattice structure with a force tolerance of 0.01 eV/Å.

Optical Band gap calculation

The absorbance measurements was collected using a CRAIC 20/30 microspectrophotometer. The spectrophotometer does not have a built in integrated sphere into the system to completely cancel the scattering from the material. However, the absorbance values of the material obatined are zeroed with the bare susbtrate. The process for obtaining the band gap using Tauc plot is as follows. A relational expression put forth by Mott and, Davis, Tauc is used:[47, 53]

$$(h\nu\alpha)^{1/n} = A\,(h\nu - E_g) \qquad (1)$$

Where, *h*: Planck's constant, *v*: frequency of vibration, α: absorption coefficient, *E*g: band gap, *A*: proportional constant.

The value of the exponent n denotes the nature of the sample transition.

For indirect allowed transition n = 2, given that the β-phase FL-Sb has an indirect band gap (from the DFT calculations).

Supporting Information

Supporting Information is available from the Wiley Online Library or from the author.

Acknowledgements

This work was performed in part at the Micro Nano Research Facility (MNRF) in the Victorian Node of the Australian National Fabrication Facility (ANFF). Facilities and technical support from the RMIT Microscopy and Microanalysis Facility, a node of Microscopy Australia, is acknowledged. We acknowledge funding from the Australian Research Council through LE150100001, and DP170103477. Scholarship support from the Research Training Program (RTP) scheme of the Australian government is acknowledged (SK). This work was supported by the Multi-modal Australian Sciences Imaging and Visualization Environment (MASSIVE) (www.massive.org.au). The theoretical calculations was undertaken with the assistance of resources and services from the National

Computational Infrastructure (NCI) supported by the Pawsey Supercomputing Centre with funding from the Australian Government and the Government of Western Australia.

Received: ((will be filled in by the editorial staff))
Revised: ((will be filled in by the editorial staff))
Published online: ((will be filled in by the editorial staff))

References

[1] Balendhran, S.; Walia, S.; Nili, H.; Sriram, S.; Bhaskaran, M., *Small.***2015,** *11*, 6

[2] Ares, P.; Aguilar‐Galindo, F.; Rodríguez‐San‐Miguel, D.; Aldave, D. A.; Díaz‐Tendero, S.; Alcamí, M.; Martín, F.; Gómez‐Herrero, J.; Zamora, F., *Adv Mater.***2016,** *28*, 30

[3] Viti, L.; Hu, J.; Coquillat, D.; Knap, W.; Tredicucci, A.; Politano, A.; Vitiello, M. S. J. A. M., *Adv Mater.***2015,** *27*, 37

[4] Zhang, S.; Zhou, W.; Ma, Y.; Ji, J.; Cai, B.; Yang, S. A.; Zhu, Z.; Chen, Z.; Zeng, H., *Nano Lett.***2017,** *17*, 6

[5] Ares, P.; Palacios, J. J.; Abellán, G.; Gómez‐Herrero, J.; Zamora, F., *Adv Mater.***2018,** *30*, 2

[6] Kuriakose, S.; Ahmed, T.; Balendhran, S.; Bansal, V.; Sriram, S.; Bhaskaran, M.; Walia, S., *2D Mater.***2018,** *5*, 3

[7] Li, L.; Yu, Y.; Ye, G. J.; Ge, Q.; Ou, X.; Wu, H.; Feng, D.; Chen, X. H.; Zhang, Y., *Nat Nanotechnol.***2014,** *9*, 5

[8] Zhang, S.; Yan, Z.; Li, Y.; Chen, Z.; Zeng, H., *Angew Chem.***2015,** *127*, 10

[9] Wang, G.; Pandey, R.; Karna, S. P., *ACS Appl Mater Interfaces.***2015,** *7*, 21

[10] Aktürk, O. Ü.; Özçelik, V. O.; Ciraci, S., *Phys Rev B.***2015,** *91*, 23

[11] Shi, Z. Q.; Li, H.; Yuan, Q. Q.; Song, Y. H.; Lv, Y. Y.; Shi, W.; Jia, Z. Y.; Gao, L.; Chen, Y. B.; Zhu, W. J. A. M., *Adv Mater.***2019,** *31*, 5

[12] Singh, D.; Gupta, S. K.; Sonvane, Y.; Lukačević, I., *J Mater Chem C.***2016,** *4*, 26

[13] Zhang, S.; Guo, S.; Chen, Z.; Wang, Y.; Gao, H.; Gómez-Herrero, J.; Ares, P.; Zamora, F.; Zhu, Z.; Zeng, H., *Chem Soc Rev.***2018,** *47* 3

[14] Mao, Y.-H.; Zhang, L.-F.; Wang, H.-L.; Shan, H.; Zhai, X.-F.; Hu, Z.-P.; Zhao, A.-D.; Wang, B., *Front Phys.***2018,** *13*, 3

[15] Wu, X.; Shao, Y.; Liu, H.; Feng, Z.; Wang, Y. L.; Sun, J. T.; Liu, C.; Wang, J. O.; Liu, Z. L.; Zhu, S. Y., *Adv Mater.***2017,** *29*, 11

[16] Fortin-Deschênes, M.; Waller, O.; Mentes, T.; Locatelli, A.; Mukherjee, S.; Genuzio, F.; Levesque, P.; Hébert, A.; Martel, R.; Moutanabbir, O., *Nano Lett.***2017,** *17*, 8

[17] Shao, Y.; Liu, Z.-L.; Cheng, C.; Wu, X.; Liu, H.; Liu, C.; Wang, J.-O.; Zhu, S.-Y.; Wang, Y.-Q.; Shi, D.-X., *Nano Lett.***2018,** *18*, 3

[18] Ji, J.; Song, X.; Liu, J.; Yan, Z.; Huo, C.; Zhang, S.; Su, M.; Liao, L.; Wang, W.; Ni, Z., *Nat Comm.***2016,** *7*, 1

[19] Gibaja, C.; Rodriguez‐San‐Miguel, D.; Ares, P.; Gómez‐Herrero, J.; Varela, M.; Gillen, R.; Maultzsch, J.; Hauke, F.; Hirsch, A.; Abellán, G., *Angew. Chem. Int. Ed.***2016,** *55*, 46

[20] Wang, X.; Song, J.; Qu, J., *Angew Chem Int.***2019,** *58*, 6

[21] Wang, G.; Pandey, R.; Karna, S. P. J. A. a. m.; interfaces, *ACS Appl. Mater. Interfaces.***2015,** *7*, 21

[22] Ji, L.-J.; Qin, Y.; Gui, D.; Li, W.; Li, Y.; Li, X.; Lu, P. J. C. o. M., *Chem of Mater.***2018,** *30*, 24

[23] Sun, X.; Lu, Z.; Xiang, Y.; Wang, Y.; Shi, J.; Wang, G.-C.; Washington, M. A.; Lu, T.-M., *ACS nano.***2018**, *12*,6

[24] Lei, T.; Liu, C.; Zhao, J.-L.; Li, J.-M.; Li, Y.-P.; Wang, J.-O.; Wu, R.; Qian, H.-J.; Wang, H.-Q.; Ibrahim, K., *J of Appl Phys.***2016,** *119*, 1

[25] Dobkin, D.; Zuraw, M. K., *Principles of chemical vapor deposition*. Springer Science & Business Media: **2003**.

[26] Yang, Y.; Pu, H.; Di, J.; Zhang, S.; Hu, J.; Zang, Y.; Gao, C.; Chen, C., *AIP Advances.***2018,** *8*, 8

[27] Zhang, L.; Liu, K.; Wong, A. B.; Kim, J.; Hong, X.; Liu, C.; Cao, T.; Louie, S. G.; Wang, F.; Yang, P. J. N. l., *Nano Lett.***2014,** *14*, 11

[28] Wang, X.; Zhang, Y. P.; Chen, Z. Q. J. M. R. E., *Mater. Res. Express.***2016,** *3*, 6

[29] Cheng, Y.; Wang, Y.; Zheng, Y.; Qin, Y. J. T. J. o. P. C. B., *J. Phys. Chem. B.***2005,** *109*, 23

[30] Zhou, D.; Shu, H.; Hu, C.; Jiang, L.; Liang, P.; Chen, X. J. C. G.; Design, *Cryst. Growth Des.***2018,** *18*, 2

[31] Walsh, L. A.; Hinkle, C. L., *Appl Mater Today.***2017,** *9*,

[32] Thornton, J. A. J. A. r. o. m. s., *Annu Rev Mater Sci.***1977,** *7*, 1

[33] Harris, S. J.; Weiner, A. M. J. J. o. a. p., *J of Appl Phys.***1994,** *75*, 10

[34] Regmi, M.; Chisholm, M. F.; Eres, G. J. C., *Carbon.***2012,** *50*, 1

[35] Dimitriadis, C.; Stoemenos, J.; Coxon, P.; Friligkos, S.; Antonopoulos, J.; Economou, N. J. J. o. a. p., *J of Appl Phys.***1993,** *73*, 12

[36] Lannin, J.; Calleja, J.; Cardona, M. J. P. R. B., *Phys Rev B.***1975,** *12*, 2

[37] Wang, X.; He, J.; Zhou, B.; Zhang, Y.; Wu, J.; Hu, R.; Liu, L.; Song, J.; Qu, J., *Angew Chem Int.***2018,** *130*, 28

[38] Peng, L.; Ye, S.; Song, J.; Qu, J., *Angew Chem Int.***2019,** *58*, 29

[39] Tang, X.; Hu, L.; Fan, T.; Zhang, L.; Zhu, L.; Li, H.; Liu, H.; Liang, J.; Wang, K.; Li, Z., *Adv Funct Mater.***2019,** *29*, 15

[40] Gao, Y.; Tian, W.; Huo, C.; Zhang, K.; Guo, S.; Zhang, S.; Song, X.; Jiang, L.; Huo, K.; Zeng, H., *J Mater Chem A.***2019,** *7*, 7

[41] Huang, C.; Gholipour, B.; Knight, K.; Ou, J.; Hewak, D. J. A. i. O., *Adv OptoElectronics.***2012,** *2012*,

[42] Hong, K.-S.; Nam, D.-H.; Lim, S.-J.; Sohn, D.; Kim, T.-H.; Kwon, H. J. A. a. m.; interfaces, *ACS Appl. Mater. Interfaces.* **2015,** *7*, 31

[43] Yang, X.; Ma, J.; Wang, H.; Chai, Y.; Yuan, R. J. M. C.; Physics, *Mater Chem Phys.***2018,** *213*,

[44] Gopalakrishnan, P.; Manohar, H., *J Solid State Chem.***1975,** *15*, 1

[45] Wang, Y.; Huang, W.; Wang, C.; Guo, J.; Zhang, F.; Song, Y.; Ge, Y.; Wu, L.; Liu, J.; Li, J. J. L., *Laser Photonics Rev.***2019,** *13*, 4

[46] Barrett, C.; Cucka, P.; Haefner, K. J. A. C., *Acta Crystallographica.***1963,** *16*, 6

[47] Su, L.; Tang, X.; Fan, X.; Ma, D.; Liang, W.; Li, Y.; Zhang, H. J. A. F. M., *Adv Funct Mater.***2019,** *29*, 45

[48] Lee, C.; Yan, H.; Brus, L. E.; Heinz, T. F.; Hone, J.; Ryu, S. J. A. n., *ACS nano.***2010,** *4*, 5

[49] Li, H.; Zhang, Q.; Yap, C. C. R.; Tay, B. K.; Edwin, T. H. T.; Olivier, A.; Baillargeat, D. J. A. F. M., *Adv Funct Mater.***2012,** *22*, 7

[50] Kresse, G.; Furthmüller, J., *J Phys. Rev. B.***1996,** *54*, 11

[51] Perdew, J. P.; Burke, K.; Ernzerhof, M. J. P. r. l., *Phys Rev Lett.***1996,** *77*, 18

[52] Blöchl, P. E. J. P. r. B., *Phys Rev B.***1994,** *50*, 24

[53] Li, X.; Zhu, H.; Wei, J.; Wang, K.; Xu, E.; Li, Z.; Wu, D. J. A. P. A., *Appl. Phys. A.***2009,** *97*, 2

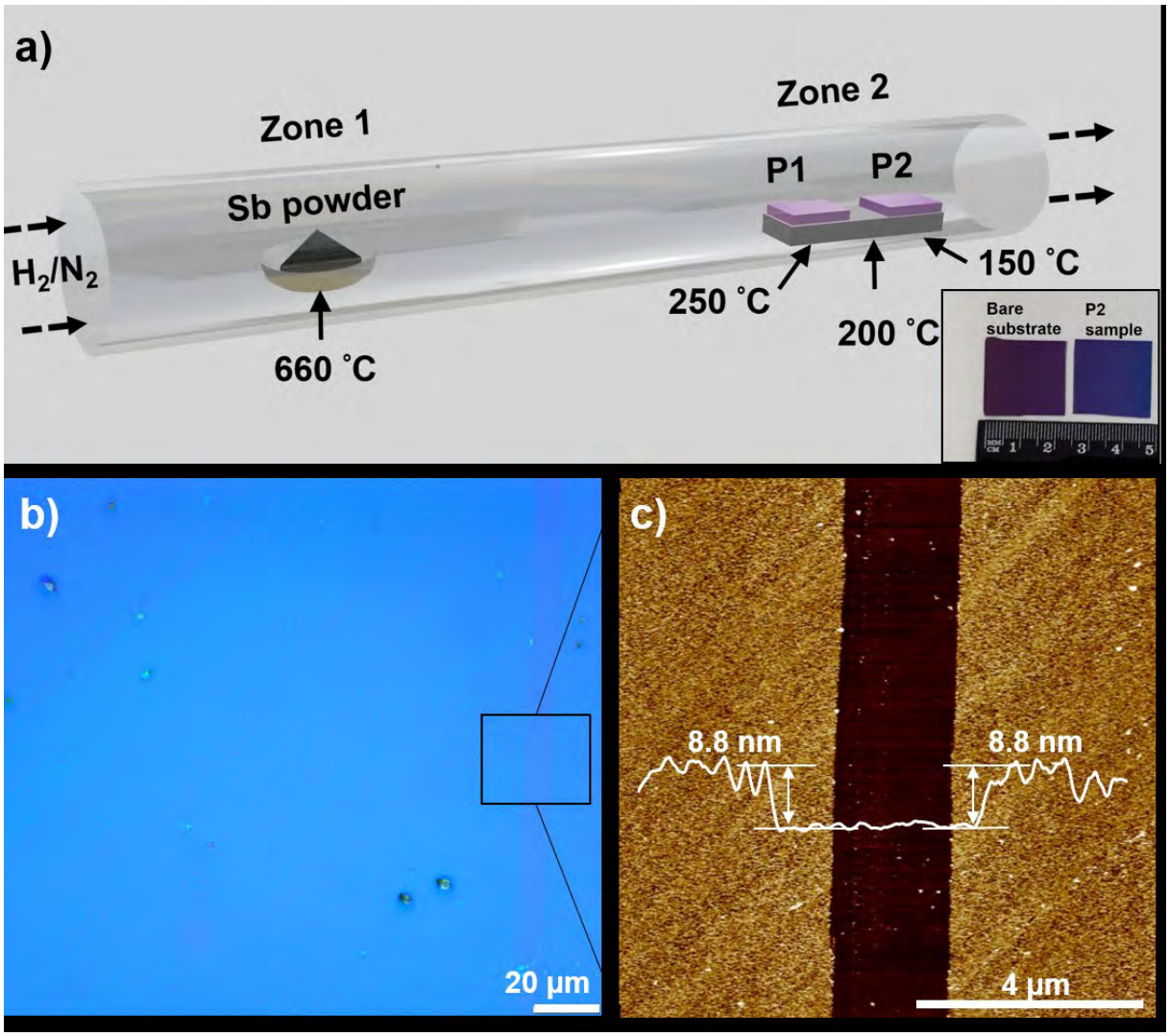

Figure 1. (a) A schematic illustration of the synthesis process indicating the sample positions and their respective temperatures. The inset is the optical image of large aspect ratio of grown antimonene nanosheets on SiO_2/Si in comparison with a bare SiO_2/Si substrate (substrates size ~2.2 x 2.2 cm^2). (b) A microscopic image of the as-grown large area from P2 (Position 2, in (a)). (c) Atomic force micrograph of the area indicated in (b) and inset of the corresponding thickness profile.

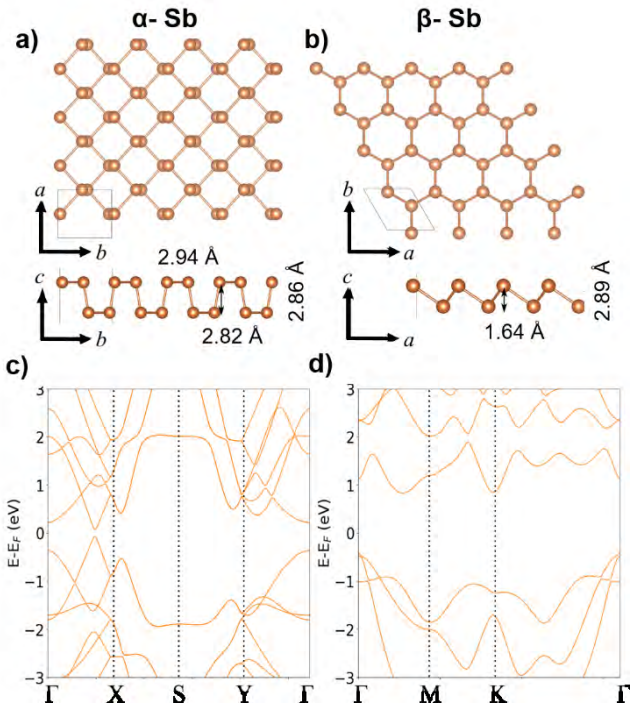

Figure 2. DFT calculations: The relaxed atomic structure of (a) α-Sb and (b) β-Sb. The calculated band structure of (c) α-Sb and (d) β-Sb.

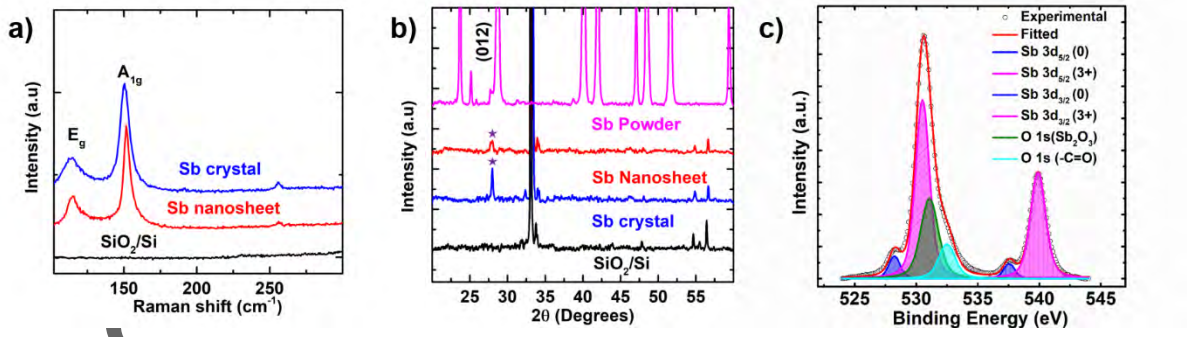

Figure 3. (a) Raman spectra of the as-grown antimonene (single crystal and large area nanosheets) on SiO_2/Si substrates. (b) The X-ray diffractograms of the as-grown crystals and nanosheets compared with the bulk powder used as precursor. The Sb (012) plane is indicated by a star. (c) De-convoluted XPS core-level spectra of the as-grown FL-Sb on Au-coated Si substrate, revealing the antimonene peaks in the material along with native surface oxide.

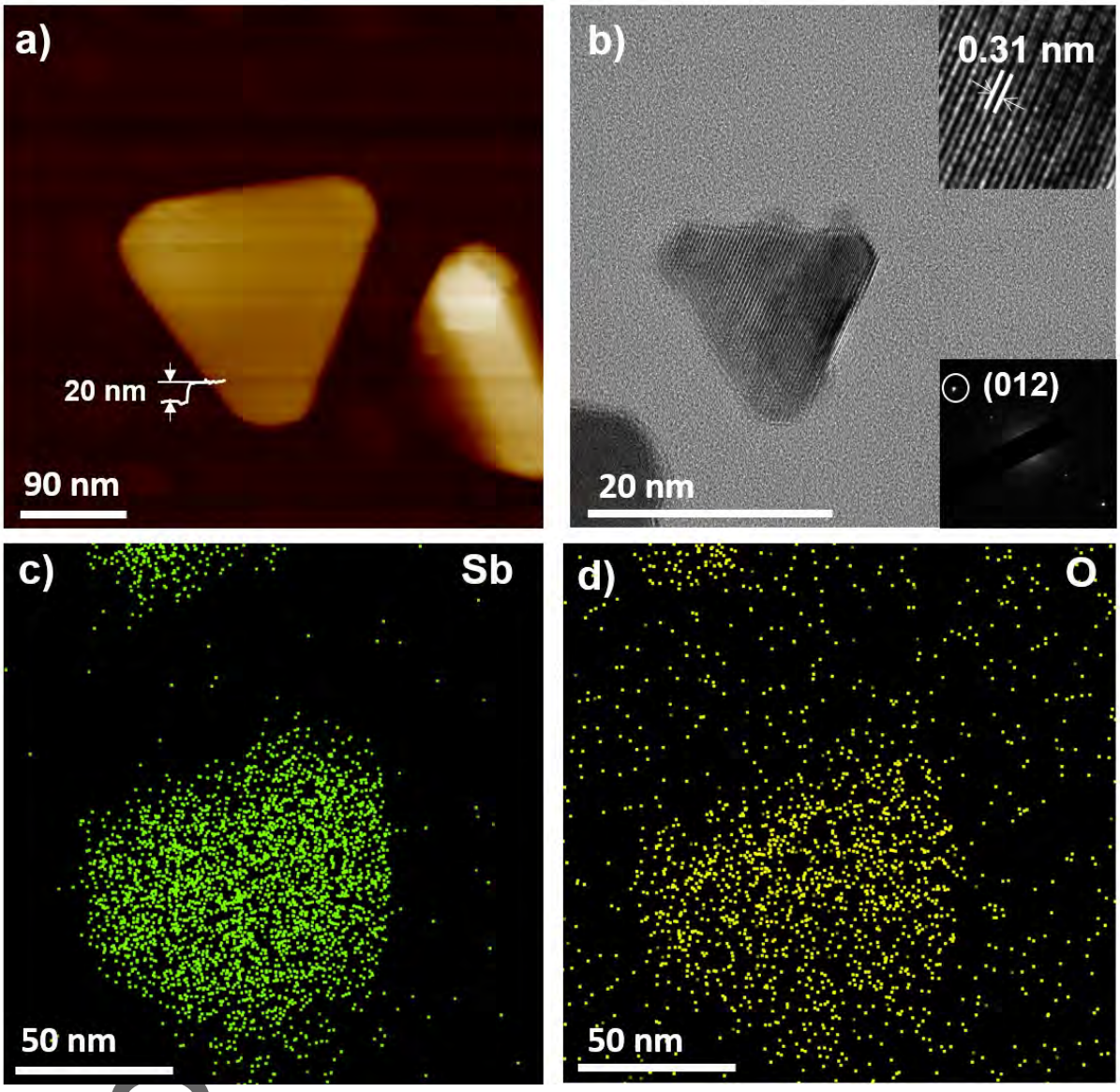

Figure 4. (a) AFM image of an antimonene crystal grown on SiO_2 substrate with its corresponding thickness profile. (b) The HRTEM image of an antimonene crystal grown directly on the SiN grids with insets showing the lattice spacing and SAED patterns. (c, d) The antimony and oxygen EDS maps of the antimonene crystals grown on SiN.

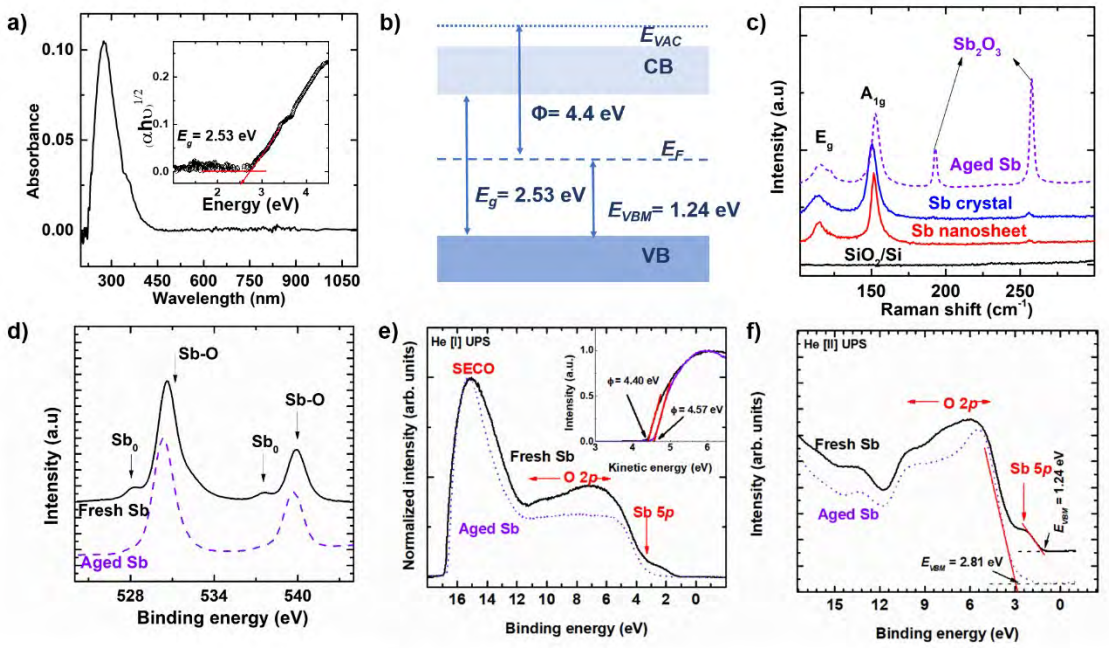

Figure 5. (a)The absorption spectra of the FL-Sb with the inset showing the bandgap measurement using Tauc plot. (b) The schematic of the band diagram of FL-Sb with the optical bandgap and the valence band minimum from the UPS experiments. Stability of the freshly grown FL-Sb is compared with an aged sample (9 months) (c) The comparison of the Raman spectra shows a red shift and prominent oxide peaks (d) The XPS data of the aged sample shows only the oxide peaks showing that the samples are not stable as reported in previous studies. (e,f) show the UPS curves of the FL- Sb with their valence band maximum and work function values obtained from the experimental run.

Synthesis of high aspect-ratio mono-crystalline antimonene via physical vapour deposition is shown in this study. This direct synthesis technique is a step towards unravelling the properties and practical applications of this material, across a wide range of fields of research.

Sruthi Kuriakose, Shubhendra Kumar Jain, Sherif A. Tawfik, Michelle J.S Spencer, Billy J. Murdoch, Mandeep Singh, Fahmida Rahman, Edwin LH Mayes, Mohammad Yousef Taha,[†] Rajour Tanyi Ako, Vipul Bansal, Taimur Ahmed, Sharath Sriram, Madhu Bhaskaran, Sivacarendran Balendhran[††]* and Sumeet Walia[†††]*

Mono-crystalline antimonene nanosheets via physical vapour deposition